Title

Correlating chemistry and mass transport in sustainable iron production.

Permalink

https://escholarship.org/uc/item/0sf4f309

Journal

Proceedings of the National Academy of Sciences, 120(43)

Authors

Zheng, Xueli
Paul, Subhechchha
Moghimi, Lauren
et al.

Publication Date

2023-10-24

DOI

10.1073/pnas.2305097120

Peer reviewed

Correlating chemistry and mass transport in sustainable iron production

Xueli Zheng[a,b], Subhechchha Paul[a,c] (ID), Lauren Moghimi[a,c] (ID), Yifan Wang[a,c] (ID), Rafael A. Vilá[a], Fan Zhang[d], Xin Gao[a], Junjing Deng[e] (ID), Yi Jiang[e], Xin Xiao[a], Chaolumen Wu[f] (ID), Louisa C. Greenburg[a], Yufei Yang[a], Yi Cui[a], Arturas Vailionis[a], Ivan Kuzmenko[e], Jan Ilavsky[e] (ID), Yadong Yin[f], Yi Cui[a,b], and Leora Dresselhaus-Marais[a,b,c,g,1] (ID)

Steelmaking contributes 8% to the total CO_2 emissions globally, primarily due to coal-based iron ore reduction. Clean hydrogen-based ironmaking has variable performance because the dominant gas–solid reduction mechanism is set by the defects and pores inside the mm- to nm-sized oxide particles that change significantly as the reaction progresses. While these governing dynamics are essential to establish continuous flow of iron and its ores through reactors, the direct link between agglomeration and chemistry is still contested due to missing measurements. In this work, we directly measure the connection between chemistry and agglomeration in the smallest iron oxides relevant to magnetite ores. Using synthesized spherical 10-nm magnetite particles reacting in H_2, we resolve the formation and consumption of wüstite ($Fe_{1-x}O$)—the step most commonly attributed to whiskering. Using X-ray diffraction, we resolve crystallographic anisotropy in the rate of the initial reaction. Complementary imaging demonstrated how the particles self-assemble, subsequently react, and grow into elongated "whisker" structures. Our insights into how morphologically uniform iron oxide particles react and agglomerate in H_2 reduction enable future size-dependent models to effectively describe the multiscale aspects of iron ore reduction.

materials science | sustainability | extractive metallurgy | hydrogen-based direct reduction | nanochemistry

Steel is ubiquitous in modern society, but its production contributes to 8% of global CO_2 emissions (1–3). More than half of the CO_2 emitted in steelmaking occurs when reducing the iron oxide ores into molten iron. Ironmaking is done predominantly using blast furnaces that use processed coal to form carbonaceous reducing agents (C and CO) in-process that generate vast CO_2 emissions (4, 5). Gas injection has been exploited to reduce coal requirements and CO_2 emissions, but coal is always required for blast-furnace ironmaking. Efforts have emerged to use natural gas (6, 7), electrochemistry (8), and hydrogen gas (9, 10) for cleaner ironmaking, but those only make up ~5% of the global market today (11).

Hydrogen-based direct reduction (HyDR) of iron ores is a different approach to ironmaking that replaces coal with H_2 gas, generating H_2O instead of CO_2. While seemingly simple, the HyDR process has been slow to commercialize because of its endothermic chemistry, which requires the reaction to be operated at higher temperatures (12). However, high temperature causes the iron ores and product iron to agglomerate and clog the reactors due to a process called whiskering (13–15). Models of the whiskering process are known to be essential to effectively scale HyDR, but the high variability between different ores and local reactor conditions has yielded challenges in accuracy (9, 16).

It has been shown that accurate models must describe both the microstructure and chemistry of the reduction over time (3, 17). HyDR reactors typically operate at 800 to 1,000 °C, but the endothermic reaction causes microscopic temperature fluctuations inside the macroscopic vessels that change the local structure (15). Industrial ironmaking converts hematite (Fe_2O_3) ores into magnetite (Fe_3O_4) then wüstite ($Fe_{1-x}O$) and finally iron (Fe), with the rate-limiting step being the $Fe_{1-x}O$ to Fe transition (18, 19). The proposed surface-based (topochemical) mechanism of wüstite to iron conversion is the depletion of substoichiometric oxygen (via diffusion) until it reaches a critical threshold to nucleate regions of the Fe phase (20). Several groups have observed kinetics differences at surface-based defects, i.e., boundaries between phases and grains, which is consistent with the topochemical models (15, 21). By contrast, early work demonstrated the reduction rate of iron oxide ores also depends strongly on the evolution of internal pores even in initially dense samples (22); similar findings have emerged more recently (23). Each step of the reactions significantly reduces the volume of the material,

Significance

Steel is an essential material of the modern world, but its production accounts for ~8% of the global CO_2 footprint, half of which occurs from converting iron ores (oxides) into molten iron. Hydrogen-based reduction of iron ores (HyDR) offers green "ironmaking," but scaling it to megatonne/yr throughput requires science to decouple the reduction kinetics and sintering. Our study reveals the importance of the smallest nanoscale particles intrinsic to iron ores in nucleating the "sticking" processes at previously unexplored temperatures. By resolving how the crystal packing and self-assembly of oxide particles couple to sintering that is known to mitigate the efficiency of clean ironmaking reactors, our experiments lay the foundations and need for multiscale HyDR chemistry.

generating new defects that alter the rates of subsequent reduction steps.

Whiskering is known to proceed by first overcoming a relatively high activation energy to nucleate then continuing via a lower-energy growth mechanism (24). As such, the whiskering process is highly dependent on small distortions that seed further accumulation. Understanding the anomalous low-temperature mechanisms through which the local kinetics may link to whiskering is essential to design efficient reactors. To date, studies have characterized these relations in the mm-scale "pellets" used in most of today's reactors, but the refined iron ores, or "fines," consolidate the process using <100-μm-sized particles. In all cases, the smallest particles cause unexpected reactor failures. In pellet reactors, collisions between particles typically produce a dust called "pellet fines" that can enhance whiskering (25), while fines reactors observe defluidization from smaller particles (26). Submicrometer particles in iron ore reduction have been shown to be prevalent in most reactors today but are typically overlooked in reactor design models.

In this work, we present a multiscale view of HyDR chemistry using nanoparticles with advanced microscopy and scattering methods to directly map the formation of wüstite and then iron and its link to whiskering. We study pure iron oxide particles at nm-scales representative of the smallest particles in industrial iron ore fines. For comparison, we used controlled lab-synthesized 10-nm particles and compared them to industrial magnetite ore fines with H_2 reduction. Using in situ X-ray diffraction (XRD), we demonstrate the kinetics of the two steps of reduction ($Fe_3O_4 \rightarrow Fe_{1-x}O$, then $Fe_{1-x}O \rightarrow Fe$) and observe unexpected $Fe_{1-x}O$ phase formation at 300 °C, despite the previously reported thermodynamic instability of the phase. Our results indicate that the formation and consumption of wüstite involve reaction rates that differ depending on the orientation and energy of each crystallographic surface (facet) at 300 °C. Simultaneous small-angle X-ray scattering (SAXS) indicated that

as the reduction occurs, the particle sizes dramatically increase, suggesting the onset of a sintering process. Images of our samples by transmission electron microscopy (TEM) and X-ray ptychographic tomography at the nano/microscopic scales reveal a complex hierarchical organizational process that illustrates the occurrence of whiskering even in the absence of the bulk crystals they usually agglomerate. Our study of pristine iron oxide nanoparticles affords a unique view of how chemistry links to multiscale mechanics in the absence of any impurities, initial porosity, or shape effects. This insight provides a key starting point to connect length scales in models to design and optimize different HyDR approaches.

Results

Comparison of Industrial and Nanoparticle Magnetite Reduction.
It is challenging to connect the chemistry of the industrial reaction between the nano- and micro-scales due to complexity of the reaction caused by the defects in natural samples. Therefore, we begin by comparing magnetite concentrate samples extracted from the Mesabi Range in Minnesota to lab-synthesized Fe_3O_4 nanoparticles in order to confirm the appropriate scale of nanoscale chemistry that is representative of the industrial fines. The scanning electron microscopy (SEM) images of industrial iron ore fines (Fe_3O_4) shown in Fig. 1A display the wide range of particle size distributions from nanoscale to microscale (additional images shown in *SI Appendix*, Fig. S1). In comparison, we synthesized uniform spherical Fe_3O_4 nanoparticles with a 10-nm diameter (Fig. 1D). For the solid–gas reaction, XRD measures the phase transformations based on the amount of each crystal structure observed, as shown in Fig. 1. We performed in situ XRD for these reductions in an isothermal reactor at T = 800 °C using 2% H_2/Ar for industrial fines (Fig. 1B) and nanoparticle (Fig. 1E) Fe_3O_4. In situ XRD showed the reduction of magnetite (Fe_3O_4) to wüstite ($Fe_{1-x}O$), and subsequently $Fe_{1-x}O$ to Fe. We observed the phase
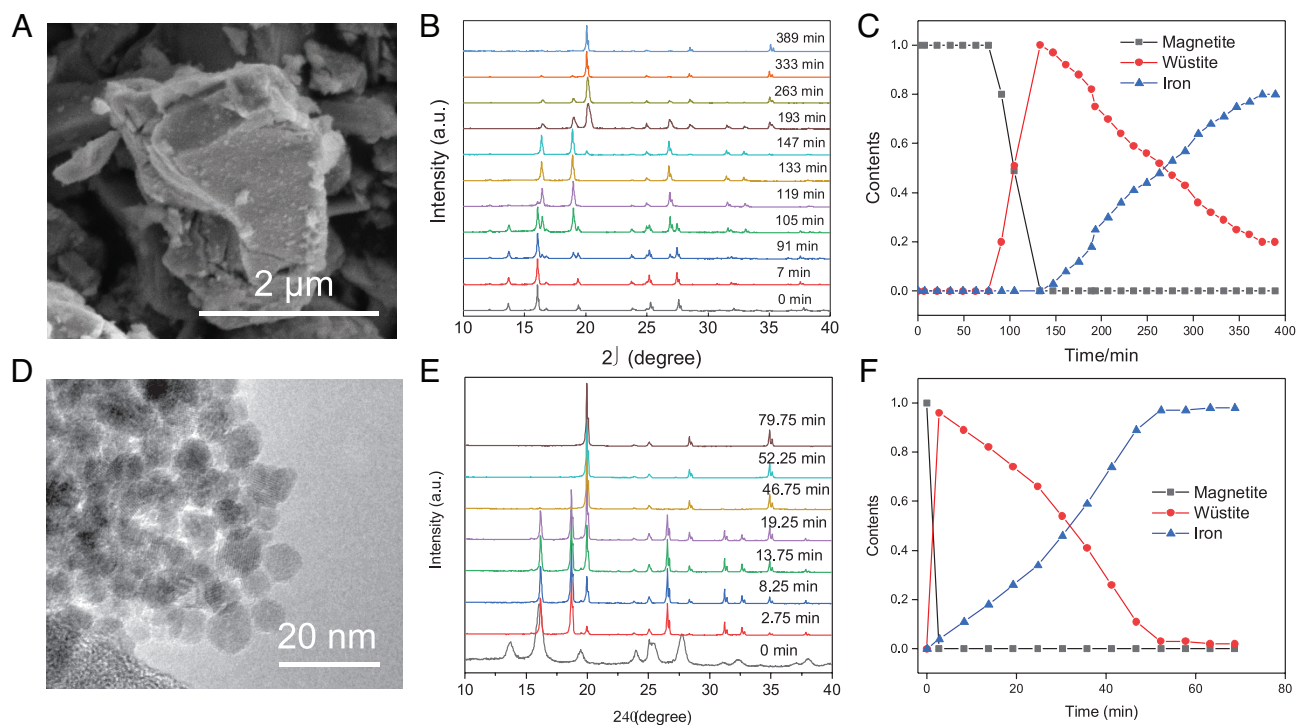
Fig. 1. Morphology and reaction kinetics of (*A–C*) industrial Fe_3O_4 and (*D–F*) nanoscale Fe_3O_4. (*A*) Scanning electron microscopy (SEM) image of industrial Fe_3O_4 and (*D*), TEM of nanoscale Fe_3O_4. In situ XRD of (*B*) industrial Fe_3O_4 and (*E*) nanoscale Fe_3O_4. Phase fraction of magnetite, wüstite, and iron for (*C*) industrial Fe_3O_4 and (*F*) nanoscale Fe_3O_4 derived from in situ XRD results. The uncertainty for the analysis is less than 3%.

fractions of Fe_3O_4, $Fe_{1-x}O$, and Fe for industrial Fe_3O_4 (Fig. 1C) and nanoparticle Fe_3O_4 (Fig. 1F). Mapping the XRD signal, we observed a rapid reduction of Fe_3O_4 to $Fe_{1-x}O$ for both industrial Fe_3O_4 (Fig. 1C) and nanoscale Fe_3O_4 (Fig. 1F). Phase fraction results revealed the fast reduction from Fe_3O_4 to $Fe_{1-x}O$. The rate-limiting step was the reduction of $Fe_{1-x}O$ to metallic Fe for both industrial Fe_3O_4 and nanoscale Fe_3O_4. Our industrial Fe_3O_4 fines exhibited an initial lag time for the first 90 min at 800 °C (Fig. 1C), indicating slow hydrogen diffusion rates in the industrial Fe_3O_4.

Iron reduction kinetics is known to exhibit strong dependence on the rates of adsorption and diffusion of reactive species. The initial reaction begins with H_2 surface adsorption and bond cleavage (27), but progresses via oxygen atom diffusion toward the surface along the kinetically favored directions (following Fick's laws) (28). Studies have observed that the $Fe_{1-x}O$ phase's metastability causes it to proceed via Fe_2O_3 to Fe_3O_4 to Fe at temperatures below 570 °C, while passing through $Fe_{1-x}O$ intermediates between Fe_3O_4 and Fe at higher temperatures. Our Fe_3O_4 nanoparticles had much faster reaction rates, with the majority of nanoscale Fe_3O_4 being reduced to $Fe_{1-x}O$ at 800 °C within 3 min (Fig. 1F). As such, for a mechanistic picture to compare with established literature, we explored this chemistry at lower temperatures, using synchrotron-based approaches.

Low-Temperature Reduction of Nanoscale Fe_3O_4. The high X-ray flux and efficient X-ray detection at the Advanced Photon Source allowed us to resolve the low-temperature formation

and consumption of $Fe_{1-x}O$ quite clearly, using the setup shown schematically in Fig. 2A (29). Representative XRD traces from our experiment at 300 °C are plotted in Fig. 2B, with markers at the bottom indicating the representative positions of the diffraction peaks characteristic of each phase. We unexpectedly observed the $Fe_{1-x}O$ phase forms preferentially in all reactions observed, even down to 300 °C. Many studies thus far have demonstrated that the $Fe_{1-x}O$ phase is thermodynamically unstable below 570 °C (30), though its kinetics compete with the low-temperature $Fe_3O_4 \rightarrow$ Fe reaction over a range of 450 to 570 °C (16). Our observation of the preferred formation of $Fe_{1-x}O$ down to 300 °C indicates that nanoparticles further kinetically prefer or stabilize this phase beyond previous findings (31, 32). Since previous size-dependent thermodynamic studies revealed that the surface to volume ratio should destabilize the wüstite phase (33), we hypothesize that this may be caused by kinetic effects, such as a lower transition state energy due to the size effects, for this pathway.

We included a plot in Fig. 2C to compare the trends for the formation of iron at 800 °C, 350 °C, and 300 °C; our results indicated three characteristic modes of these kinetics. At intermediate temperatures (350 °C), we observed a gradual conversion to iron, following a roughly logarithmic function, growing toward an asymptotic population from the beginning of the reaction time. At the very lowest temperature, however, we observe a lag time in the formation of metallic iron lasting ~200 min, after which the iron forms following an exponential distribution. We scale the curves collected from experiments at different temperatures
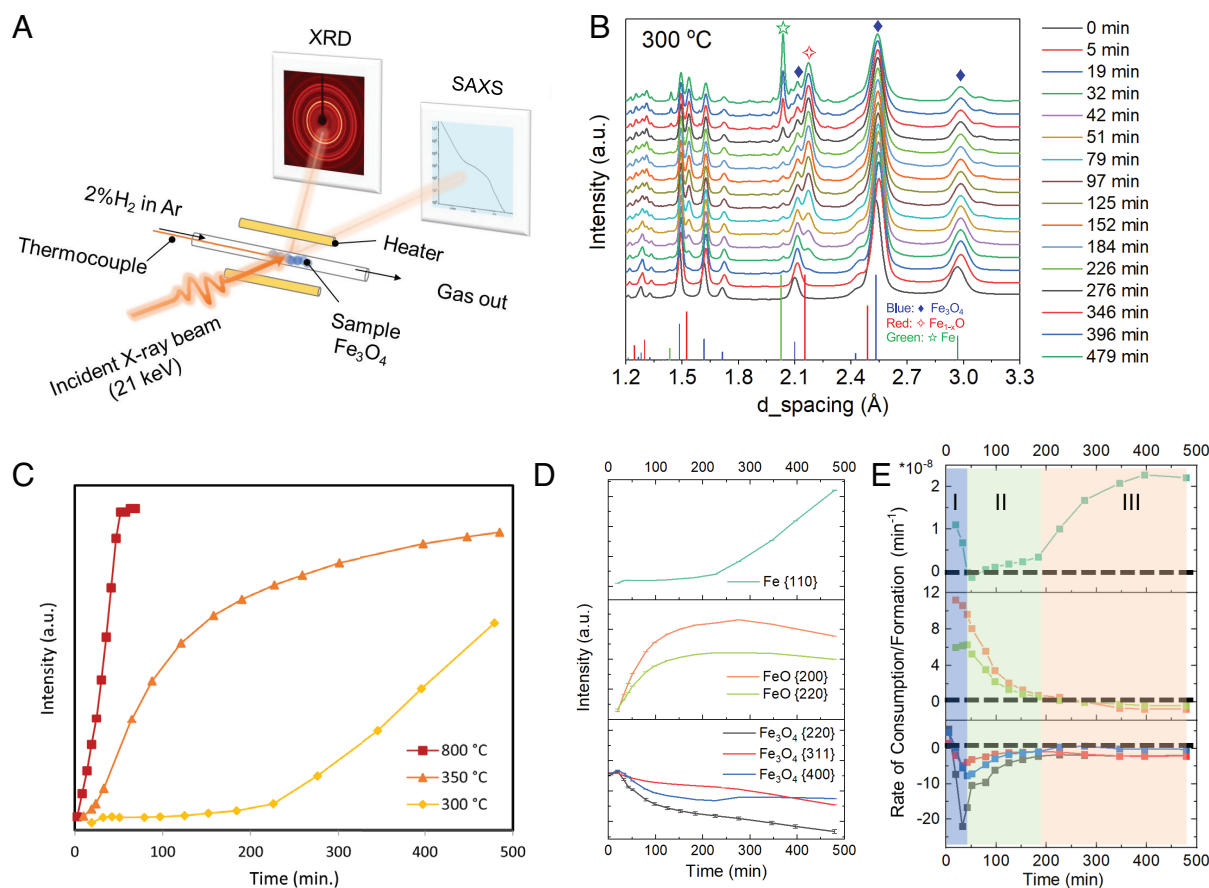

Fig. 2. Overview of in situ XRD of chemistry for Fe_3O_4 nanoparticles at 300 °C. (A) A schematic of in situ small angle X-ray scattering (SAXS), and XRD experimental configuration. (B) Representative time traces of in situ XRD showing the nanoparticle chemistry of Fe_3O_4 at 300 °C in 2% H_2 in Ar (g). (C) A plot of the formation of iron comparing our observations from 300 °C, 350 °C, and 800 °C. The uncertainty for the analysis is less than 3%. (D) The phases and facets of the anomalous 300 °C chemistry are shown by the normalized integrated intensity under the relevant {hkl} diffraction peaks. (E) The plot of the first derivative of the traces from (D), indicating the net consumption and formation of each phase and crystal plane as a function of time.

to the estimated final phase fraction of Fe to illustrate the difference in extent of chemistry.

To investigate the dramatic change to the kinetics of Fe formation at 300 °C, we study the full progression of the consumption and formation of Fe_3O_4, $Fe_{1-x}O$, and Fe, as plotted in Fig. 2D. The traces in Fig. 2D were calculated based on the area under the curve of each {hkl} peak in the XRD traces from Fig. 2B, which is related to the number of unit cells of the crystals that are oriented along that direction (c.f. the volume abundance). By taking the derivative of the area under each peak with respect to the time of the integrated intensities, we measured the rate of consumption/ formation of each phase, as shown in Fig. 2E. The plots in Fig. 2E demonstrate rates of consumption for points with negative values, and rates of formation with positive values, all with magnitudes that scale with rate. In the case of magnetite and wüstite, the reaction rates differed for different diffraction peaks, indicating that the crystallographic orientation is intrinsically linked to the mechanism and associated kinetics. For a time-evolving system and a fully isotropically oriented initial powder, the changes to the relative peak areas between {hkl} planes imply needle-like shapes emerge that enhance the amount of the phase that is oriented along a specific crystallographic direction. In our reactive system, the temporal changes to the relative area under each peak thus indicate a crystallographic dependence of the reaction. We include a full description of our normalization procedures and interpretation of the synchrotron XRD analysis in *SI Appendix, Supplementary Note 1*.

As highlighted by the blue, green, and orange boxes in Fig. 2E, we observed three distinct behaviors of the phase transition dynamics, which we interpret to be different mechanistic stages of the chemistry. Each stage is distinguished by a change in the facet dependence and changes to the overall rate of conversion between phases. Starting from the perspective of phase conversion, in stage I (the first 19 min), the Fe_3O_4 is consumed while both the $Fe_{1-x}O$ and Fe form simultaneously. In stage II, we observe the consumption of Fe_3O_4 and net formation of $Fe_{1-x}O$, with almost no change in the consumption/formation of Fe. Fe begins forming in stage III, at t = 200 min with Fe_3O_4 and $Fe_{1-x}O$ both being consumed at similar rates. Additionally, in stage I, the consumption of Fe_3O_4 is fastest along the {220} plane (gray), while the $Fe_{1-x}O$ formation is fastest along {200} (orange). By contrast, in stage II, the net rates of formation for the {200} and {220} (green) facets of $Fe_{1-x}O$ converge, while the Fe_3O_4 consumption along {220}, {311} (red), and {400} (blue) initially separate before coalescing by the start of stage III. In stage III, the rates for each crystallographic facet differ minimally for each oxide phase.

Facet-dependent rates of chemistry like we observe in stage I/ II have been observed in other systems to occur based on the surface energy, which drives a change in the chemical driving force (Gibbs free energy) that governs the kinetics of the reaction (34, 35). Magnetite's inverse spinel structure is often modeled as an Face Centered Cubic lattice of oxygen sites; this indicates surface energy trends of $\gamma_{111} < \gamma_{100} < \gamma_{110}$ (36). We project the three planes measured in Fig. 2E onto the surface planes described in the literature (*SI Appendix*, Table S1) and find fastest along {220}, intermediate along {400}, and slowest along {311} which is consistent with a trend of the highest surface energy driving the fastest kinetics. In wüstite's rock-salt structure, the surface energy trends as $\gamma_{100} < \gamma_{110}$, which indicates the {110} facet has the strongest driving force for surface chemistry. We observe the wüstite phase forms fastest along the {200} facet and slows back to zero more rapidly, which is also consistent with the surface energy trends.

We interpret that the initial formation of both $Fe_{1-x}O$ and Fe in stage I indicates rapid surface chemistry, as there are sufficient active surface oxygen atoms to react with H_2 directly with no mass transport limitations for the removal of H_2O. This quickly converts to stage II, which exhibits strong rate dependence on the facet-energy during a sustained Fe_3O_4 to $Fe_{1-x}O$ conversion, indicating the strong influence of surface energy. The role of surfaces is complex in HyDR reactions, which are known to be sensitive to many parameters (16), making the native reduction mechanisms nontrivial to establish. Despite variation in the literature, the Fe_3O_4 to $Fe_{1-x}O$ transition has precedent in being modeled as a surface-dominated reaction (30), while the $Fe_{1-x}O$ to Fe transition is usually described as diffusion-limited.

As the reaction transitions from stage II to III, the formation of Fe becomes dominant, while the reaction rate of $Fe_{1-x}O$ and Fe_3O_4 phases remains nearly constant. On the other hand, early in stage III, the net reaction rate of the $Fe_{1-x}O$ phase crosses over from net formation to net consumption. We note that while we were not able to directly measure facet dependence in the iron phase, the significant narrowing of the peak widths in XRD indicates a significant increase in the effective particle sizes based on Scherrer broadening. The loss of facet dependence in the rate of consumption for both oxide phases and associated increase in crystal sizes is reminiscent of the whiskering mechanisms observed elsewhere (37). This led us to study how the dynamics in stage III coupled to nano- to micro-scale structural changes.

Microscopic View of Stage III Magnetite Reduction. To directly map the changes in size as the nanoparticles react, we measured alternating XRD and SAXS patterns to resolve the average particle size across the measured 6-mm³ volume inside the reactor capillary. SAXS measures an integrated view of the characteristic size scales in a sample with large populations of submicrometer particles and/or voids. The SAXS progression in Fig. 3A plots in situ scattering traces collected during the Fig. 2 B–E reaction, from the start (purple) to the end, at 485 min (red). The measured values of Q correspond to $\frac{2\pi}{d}$, where d is the representative size scale of the scattering particle/void. The bump in the trace that we denote with a black arrow indicates a Guinier distribution that indicates our initial population of 10-nm diameter particles. As shown in Fig. 3A, the emergence of features at lower Q-values as the reaction time increases (shown by the red arrow) indicates the formation of larger features as the reaction progresses (~50 nm by the end of stage III). Our SAXS results indicate a size progression proceeds simultaneously with the stage III (t > 200 min) reduction chemistry in Fig. 2.

We further performed TEM measurements to see the morphology and size change of the reduced Fe_3O_4. As shown in Fig. 3 B–E, our TEM images revealed a mesoscale structuring mechanism at the particle scale for different temperatures. In all cases, we observed that the initial randomly packed nanoparticles (Fig. 3B) appear to self-assemble by the end of the reaction. For the reaction at 300 °C (Fig. 3C), this self-assembly is consistent with the modest size increase shown by SAXS because the particles sinter but retain their initial nanoparticular structure. With increasing temperatures, however, we observed a trend that the self-assembled particles appear to coalesce into ~100× larger particles (Fig. 3 D and E). While the coalescence of particles into new grains occurs to a limited extent at 350 °C, by 400 °C, it becomes the dominant effect, producing a large population of agglomerated and elongated grains of 100- to 350-nm length and 20- to 50-nm width (Fig. 3E). We include the details of our statistical analysis in *SI Appendix, Supplementary Note 3*. As our control experiments in Ar (g) formed isotropically random particle geometries at 400 °C (*SI Appendix,* Fig. S9), we interpret that the reactive H_2 gas
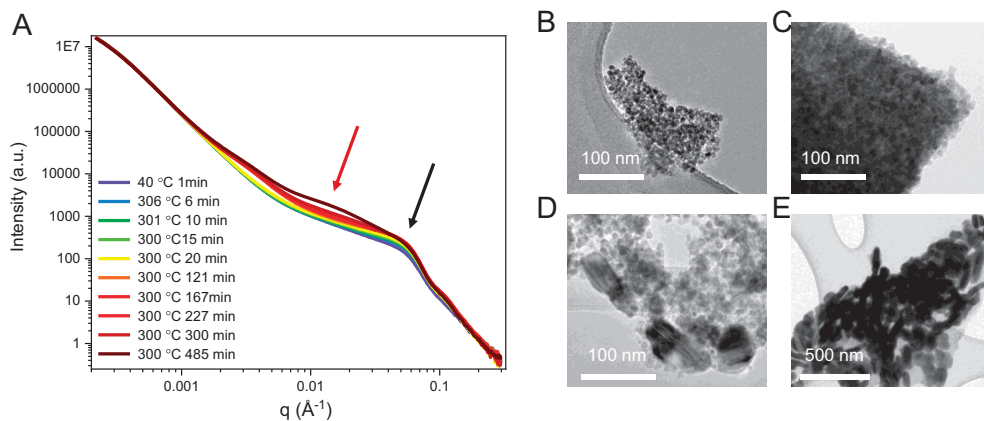
Fig. 3. Size increases measured from reactors. (*A*) In situ SAXS of reduction reaction shown in Fig. 2 for the reaction in 2% H₂ at 300 °C. TEM images of (*B*) the initial Fe₃O₄ nanoparticles, and (*C*–*E*) the final product formed after 8 h at (*C*) 300 °C, (*D*) 350 °C, and (*E*) 400 °C. All images show the products of reactions performed in 2% H₂.

and associated phase transformations cause the preferential formation of elongated structures in Fig. 3*E*. Connecting these morphological changes to the dramatic change in the Fe formation function from Fig. 2*C* leads us to conclude that a critical temperature for the competing morphological changes that seem to accelerate the reaction between 300 °C and 400 °C.

While the lower temperature reactions seem to avoid the agglomeration mechanisms, the higher temperatures used in industrial reactors led us to explore how the high-T agglomeration enhances the kinetics of Fe formation. For deeper insights into the temporal evolution of the agglomeration process, we performed ex situ imaging of samples at different stages of the reaction at 400 °C (at 0-h, 2.5-h, and 8-h). TEM images of iron oxide reacted at 400 °C for 2.5 h showed the self-assemble structure (*SI Appendix,* Fig. S11). To connect the limited statistics of our TEM data to the bulk insights offered by our in situ XRD and SAXS analysis, we performed X-ray ptychographic tomography at the same time-points as our TEM images, as shown in Fig. 4. X-ray ptychographic tomography quantifies the 3D electron density integrated over every 3D voxel of the material, with extremely high spatial resolution.

For quantitative comparison between the X-ray ptychographic tomography measurements at each reaction time, we include a histogram of the voxel electron density values for each image (Fig. 4*A*). The peaks of each histogram show the most prominent electron density values for each stage of the reaction, which is determined by the material phase in the voxel and the packing density of the particles inside the voxel. From calculations of the different possible phases and packing densities, we identify a threshold at ~1,200 e/nm³ that delineates the different packing densities of oxides from those of pure iron. For our starting material, we identify a peak (black) at ~600 e/nm³ that indicates a mean packing density of 36 Fe₃O₄ particles per voxel. We note that this is ~55% fewer particles than the highest-density close-packed structure. After t = 2.5 h, the distribution (red) becomes bimodal, indicating two dominant populations of phase/packing density in the sample. After t = 8 h, the peak (blue) of ~1,400 e/nm³ indicates the conversion to the iron product, with a continued increase in packing density in the new Fe phase. We note that the broadness of the peak likely also indicates a significantly wider variance on packing densities in iron, as well as partial re-oxidation and/or incomplete chemistry. See *SI Appendix, Supplementary Note* 4 for a full description of our ptychography analysis.

The t = 2.5-h distribution exhibits two peaks whose values of 1,045 and 1,210 e/nm³ indicate electron densities on either side

of the threshold value. While the lower valued peak indicates a high packing density of iron oxide particles (possibly fused to eliminate void space), the higher value corresponds to very low packing densities of the high-electron-density Fe phase beginning to form in small domains. From these findings, we interpret that the self-assembled particles begin the fusion/conversion process at the end of stage II, as seen by the anomalously dark regions.

The full 3D spatial maps of the packing densities of representative structures are shown for the starting material (Fig. 4*B*), the halted reaction at t = 2.5 h (Fig. 4*C*) and the sample collected after t = 8 h (Fig. 4*D*). We plot all 3D images of the reduced samples in Fig. 4 with ~1,200 e/nm³ as the color threshold from blue (oxide) to red (iron) voxels to highlight the microstructural changes associated with the Fe formation. Images in Fig. 4 show isosurfaces displaying the 3D contours of constant electron density for the highest electron density regions in the material at representative stages in reaction. We note that Fig. 4*D* is a higher resolution scan (18 nm) than the one given in the histogram, as it was required to prevent averaging of the fine features representative of the rods. The 3D structure for the blue trace from the histogram is shown in *SI Appendix,* Fig. S12. We display the increase in electron density by the color/transparency scaling shown in each figure. The initial samples show no preferred packing arrangements, as the domains of densest packing are random in size and orientation (also observed in Fig. 3*B*). In comparison, the intermediate timescale reveals many high electron-density domains, each with roughly spherical shapes that are representative of the nuclei of the Fe phase. The final image from the reaction shows rod-like linear structures that are analogous to the TEM structures in Fig. 3*E*.

Discussion

We interpret the connections between our XRD and imaging experiments by proposing a simple mechanistic model. For the anomalous early-stage magnetite reduction, we base our model on a multistep shrinking core model (35). Given the 10-nm size of our synthesized Fe₃O₄ nanoparticles, it is reasonable to assume that the gas–solid reaction undergoes a multistep shrinking core mechanism, as shown in Fig. 5 *A–D*. Stage I begins with the consumption of pure Fe₃O₄ and formation of both Fe₁₋ₓO and Fe. The product Fe₁₋ₓO and Fe are nucleating at multiple locations on the surface, as there are still abundant active oxygen sites of magnetite on the outer surface, as shown in Fig. 5*E*. At this stage,
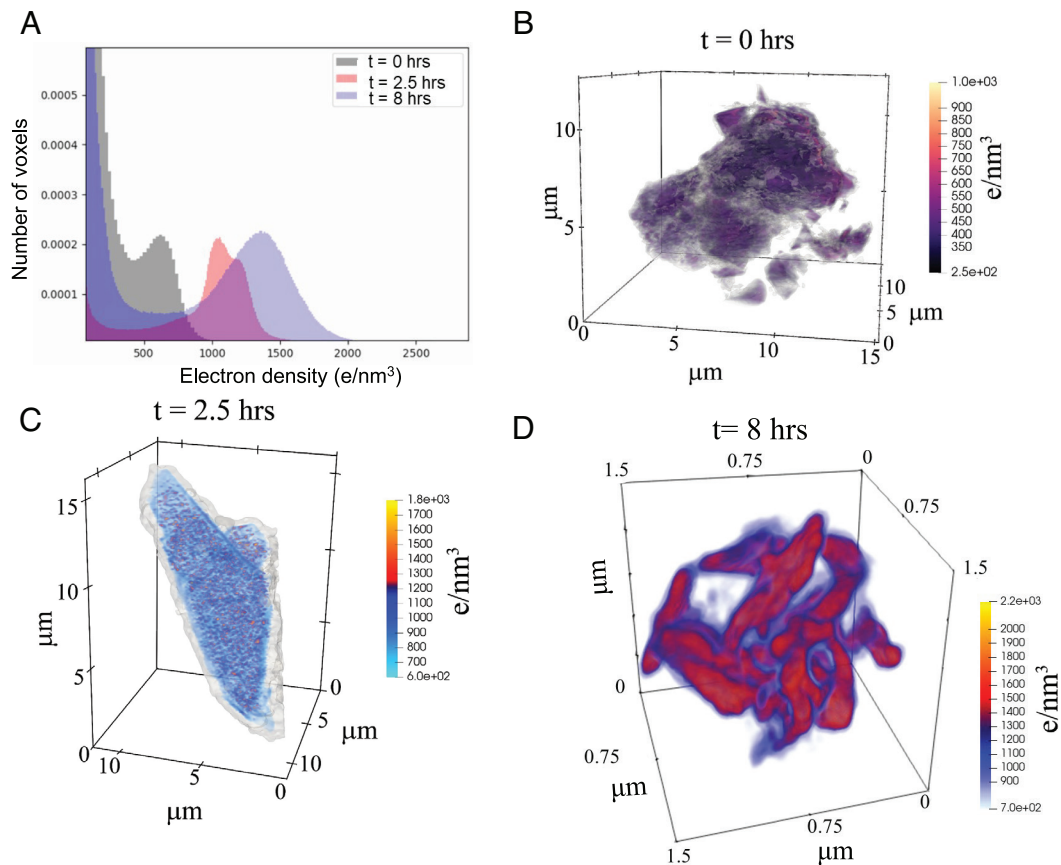
Fig. 4. X-ray ptychography of the sintering process during nano-Fe$_3$O$_4$ reduction in 2% H$_2$ in Ar at 400 °C. (*A*) Histograms of integrated voxel electron densities plotted in black, red, and blue for samples extracted after t = 0-h, t = 2.5-h, and t = 8-h. X-ray Ptychographic tomography results of (*B*) initial Fe$_3$O$_4$ nanoparticles; edge artifacts were removed for clarity (*C*) intermediate sample and (*D*) the final elongated grain structures.

the rate is governed by the surface chemical reactions, as reported by Guo et al. (38).

At the end of stage I, the nuclei of Fe$_{1-x}$O and Fe adjoin, forming a thin layer of α-Fe at the outer surface (Fig. 5*B*). At this point, there is no active oxygen on the surface, and the process is primarily driven by diffusion: Oxygen atoms, O*, formed at the Fe$_{1-x}$O-Fe surface require to diffuse through the product layer (α-Fe lattice) to reach the surface, as shown in Fig. 5*F*. This mechanism can be
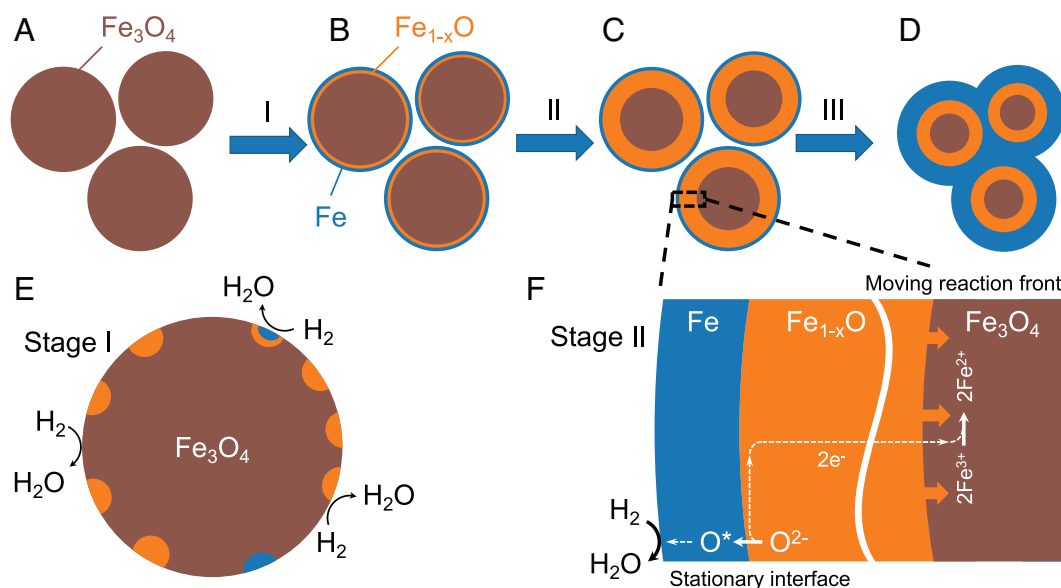

Fig. 5. (*A–D*) Schematic of our multistep shrinking-core model describing the three stages of magnetite reduction. (*D*) The final agglomeration of the nanoparticles generates macroscopic whiskers. (*E*) Stage I schematic of multiple nucleation sites for wüstite and iron on the surface of a magnetite nanoparticle. (*F*) Stage II schematic showing the only moving reaction front between wüstite and magnetite (denoted by thick orange arrows). The solid white arrows indicate the oxygen reaction and diffusion paths, and the dotted arrow indicates the electron transport direction.

validated by estimating the dimensionless Thiele number Φ^2 (39), defined as the ratio between the surface reaction rate and diffusion. We estimate the Thiele number $\Phi^2 \sim 10^{17}$ (*SI Appendix, Supplementary Note* 2), demonstrating a strong diffusion-driven mechanism at the end of stage I and during stage II.

During stage II, we observe very slow formation of Fe, but fast consumption of Fe_3O_4 and formation of $Fe_{1-x}O$, as shown in Fig. 2*E*. We propose that the overall reaction is separated into three steps and occurs simultaneously at the three interfaces (Fe surface, $Fe_{1-x}O$-Fe interface, and Fe_3O_4-$Fe_{1-x}O$ interface). The redox reaction during stage II results in the moving reaction front between the Fe_3O_4 and $Fe_{1-x}O$ phases, while the $Fe_{1-x}O$-Fe interface remains stationary, as illustrated in Fig. 5*F*. The electrons are transferred between these two interfaces, while the diffusion of the O* atoms in the Fe phase limits the overall reaction rate. An atomistic model for our proposed mechanism of electron transfer between the two reaction interfaces is discussed in *SI Appendix, Supplementary Note* 2.

As the reaction transitions from stage II to III, our ex situ TEM and ptychographic tomography observations (Figs. 3 and 4) suggest that there is a significant nanoparticle sintering at lower temperatures. We propose that the microstructure changes to the nanoparticles, thus breaking the diffusion-driven mechanism explained above. At intermediate (350 °C) to high (800 °C) temperatures, the agglomeration of the nanoparticles occurs at a higher rate. As a result, the separated stages I and II disappear at these temperatures, as corroborated by our results in Fig. 4*D*, due to competition between the fast agglomeration and the diffusional chemistry.

Previous thermodynamics models have illustrated that surface energies of iron oxides can change the relative energy stabilities of the different iron oxide phases in <100-nm particles (30, 33). In nanoparticles, the high surface to volume ratio amplifies this effect; however, the wüstite phase has been predicted to be destabilized by that effect. Our observations illustrate that despite thermodynamics, kinetic effects dominantly drive the Fe_3O_4 to $Fe_{1-x}O$ transition below the bulk stability of the $Fe_{1-x}O$ phase at 570 °C. This implies that the surface-stabilizing kinetics previously proposed extends to an even lower temperature during the Fe_3O_4 reduction in hydrogen—either due to stabilization at phase boundaries or other mechanisms.

The tubular structures in our images are characteristic of the "whiskering effect" often observed in HyDR on natural iron ore samples (37). Similarly, the facet dependence of the chemistry we observe is frequently observed in other nanoparticle systems. As we show in Fig. 1*A*, nanoparticles are present in natural iron ore fines used in industry, indicating that the unexpectedly formed $Fe_{1-x}O$ phase we observe by in situ XRD at 300 °C is relevant to anomalous cold spots generated in reactors today, though it is currently overlooked. While the nanoparticles are small, their preference for self-assembly and sintering indicates possible nucleation sites and/or barriers to the reduction that has not been explored in reactor-scale models. Nucleation sites are the highest-energy portion of most kinetic pathways and is thus essential to describe macroscopic nucleation and growth processes to connect the atomic-scale chemistry to the sintering.

Conclusions

This work studies the science underlying the coupling between chemistry and whiskering in HyDR at previously unexplored low temperatures and size scales. Our results reveal complex structuring in ribbon shapes formed by particles representative of the smallest lengthscales in iron ore fines. Our findings provide key insights into the kinetics and thermodynamics of this complex mechanochemistry

giving a perspective into scales that are necessary to model "unconventional" feedstocks (i.e., bypassing the formation of pellets). Fundamental studies like ours are essential to inform the science to optimize the chemistry and mass transport essential to design and optimize new clean ironmaking processes.

Methods

Fe_3O_4 Nanoparticle Synthesis. The Fe_3O_4 nanocrystals were synthesized by a high-temperature solution-phase hydrolysis reaction (40). NaOH stock solution (2.5 mmol/L) was prepared by dissolving 50 mmol NaOH in 20 mL diethylene glycol (DEG), followed by heating at 120 °C for 1 h under nitrogen and cooling down and keeping at 70 °C. $FeCl_3$ stock solution (0.4 mmol/L) was prepared by dissolving 8 mmol $FeCl_3$ in 20 mL DEG, followed by heating at 80 °C for 1 h and cooling down to room temperature. In a typical procedure, 288 mg polyacrylic acid (PAA), 5 mL of $FeCl_3$ stock solution, and 10 mL DEG were mixed and heated to 220 °C in a nitrogen atmosphere for 30 min under vigorous magnetic stirring, forming a transparent light-yellow solution. Then, 4.5 mL of NaOH stock solution was injected rapidly into the above hot mixture, inducing the temperature drop to 210 °C and the reaction solution turned black immediately. The resulting mixture was further heated for 10 min. Then, another 5 mL of $FeCl_3$ stock solution was injected into the above reaction. Upon the reaction temperature raised up to 220 °C, 3 mL of NaOH stock solution was added. After 15 min, Fe_3O_4 nanocrystals with a size of around 10 nm were obtained. The final products were cooled down to room temperature and washed by repeated actions of precipitation with ethanol and subsequent redispersion in deionized (DI) water several times, and finally redispersed in DI water. Fe_3O_4 nanoparticles in DI water were fully dried at 60 °C under vacuum and used as powder.

Synchrotron X-ray Measurements. In situ ultra-small angle X-ray scattering, SAXS, and XRD were carried out at beamline 9-ID-C from the Advanced Photon Source, using a photon energy of 21 keV. A mixed gas of 2% H_2 in Ar was flowed through the samples, which were packed into quartz capillaries with an inner diameter of 0.9 mm. Continuous gas flow was monitored using a bubbler, and the nanoparticles were held in place with glass wool. The temperature was controlled with an accuracy of ±5 °C with a thermocouple during the reactions.

X-ray ptychographic tomography was performed on the Velociprobe (41) located at 2-ID-D beamline at the Advanced Photon Source. Pure magnetite nanoparticles, intermediate, and final samples at the three reduction stages (t = 0, 2.5, 8 h, at 400 °C with 2% H_2 gas in Ar) were prepared on Si_3N_4 windows with a membrane thickness of 200 nm. An 8.34-keV monochromatic X-ray beam was focused by a Fresnel zone plate with an outermost zone width of 50 nm, with an illumination size of about 1.5 μm on the sample plane. Ptychographic projection scan was carried out in a raster fly-scan pattern with a horizontal step size of 150 nm and a vertical step size of 300 nm. Far-field coherent diffraction patterns were recorded by a Dectris* Eiger X 500 K detector (2.335-m downstream of the sample) at a continuous frame rate of 100 Hz. For 3D scan of each sample, 315 ptychographic projections were acquired at angles ranging from −79° to 78° with an angular step of 0.5°.

Characterization. Scanning electron microscopy images were collected using an FEI Magellan 400 XHR SEM with an field-emission gun (FEG) source. TEM images were taken at FEI Tecnai G2 F20 X-TWIN Transmission Electron Microscope with a FEG. The Empyrean X-ray Diffractometer from PANalytical was used for lab-based XRD data collection.

Data, Materials, and Software Availability. Raw data are available at https://osf.io/8mbtw/?view_only=283ed02216594786af8a117b2e90e13b (42). All other data are included in the manuscript and/or supporting information.

*Certain commercial products or company names are identified here to describe our study adequately. Such identification is not intended to imply recommendation or endorsement by the National Institute of Standards and Technology, nor is it intended to imply that the products or names identified are necessarily the best available for the purpose.

Author affiliations: [a]Department of Materials Science and Engineering, Stanford University, Stanford, CA 94305; [b]Stanford Institute for Materials and Energy Sciences, SLAC National Accelerator Laboratory, Menlo Park, CA 94025; [c]PULSE Institute, SLAC National Accelerator Laboratory, Menlo Park, CA 94025; [d]Materials Measurement Science Division, National Institute of Standards and Technology, Gaithersburg, MD 20899; [e]X-ray Science Division, Advanced Photon Source, Argonne National Laboratory, Lemont, IL 60439; [f]Department of Chemistry, University of California, Riverside, CA 92521; and [g]Department of Photon Science, SLAC National Accelerator Laboratory, Menlo Park, CA 94025

1. J. Rockström et al., A roadmap for rapid decarbonization. Science 355, 1269–1271 (2017).
2. E. Papadis, G. Tsatsaronis, Challenges in the decarbonization of the energy sector. Energy 205, 118025 (2020).
3. L. Holappa, A general vision for reduction of energy consumption and CO_2 emissions from the steel industry. Metals 10, 1117 (2020).
4. I. R. Souza Filho et al., Sustainable steel through hydrogen plasma reduction of iron ore: Process, kinetics, microstructure, chemistry. Acta Mater. 213, 116971 (2021).
5. W. Liu et al., The production and application of hydrogen in steel industry. Intern. J. Hydrogen Energy 46, 10548–10569 (2021).
6. Y. D. Wang et al., Step-wise reduction kinetics of Fe_2O_3 by CO/CO_2 mixtures for chemical looping hydrogen generation. Intern. J. Hydrogen Energy 42, 5667–5675 (2017).
7. M. N. Abu Tahari et al., Influence of hydrogen and carbon monoxide on reduction behavior of iron oxide at high temperature: Effect on reduction gas concentrations. Int. J. Hydrogen Energy 46, 24791–24805 (2021).
8. H.-G. Choi et al., Electrolysis of iron with oxygen gas evolution from molten sodium borate electrolytes. Ironmaking & Steelmaking 48, 1–8 (2021).
9. T. Wolfinger, D. Spreitzer, J. Schenk, Using iron ore ultra-fines for hydrogen-based fluidized bed direct reduction-a mathematical evaluation. Materials (Basel) 15, 3943 (2022).
10. R. Dippenaar, Industrial uses of slag (the use and re-use of iron and steelmaking slags). Ironmaking & Steelmaking 32, 35–46 (2013).
11. Z. Fan, S. J. Friedmann, Low-carbon production of iron and steel: Technology options, economic assessment, and policy. Joule 5, 829–862 (2021).
12. A. Bhaskar, M. Assadi, H. Nikpey Somehsaraei, Decarbonization of the iron and steel industry with direct reduction of iron ore with green hydrogen. Energies 13, 758 (2020).
13. K. Piotrowski, K. Mondal, T. Wiltowski, P. Dydo, G. Rizeg, Topochemical approach of kinetics of the reduction of hematite to wüstite. Chem. Eng. J. 131, 73–82 (2007).
14. Y. Yang, K. Raipala, L. Holappa, Treatise on Process Metallurgy (Elsevier, 2014), pp. 2–88.
15. S.-H. Kim et al., Influence of microstructure and atomic-scale chemistry on the direct reduction of iron ore with hydrogen at 700°C. Acta Mater. 212, 116933 (2021).
16. A. Pineau, N. Kanari, I. Gaballah, Kinetics of reduction of iron oxides by H_2. Thermochim. Acta 447, 89–100 (2006).
17. H.-Y. Lin, Y.-W. Chen, C. Li, The mechanism of reduction of iron oxide by hydrogen. Thermochim. Acta 400, 61–67 (2003).
18. K. Piotrowski et al., Effect of gas composition on the kinetics of iron oxide reduction in a hydrogen production process. Intern. J. Hydrogen Energy 30, 1543–1554 (2005).
19. K. Rechberger, A. Spanlang, A. Sasiain Conde, H. Wolfmeir, C. Harris, Green hydrogen-based direct reduction for low-carbon steelmaking. Steel Res. Int. 91, 1–10 (2020).
20. S. He et al., Direct reduction of fine iron ore concentrate in a conical fluidized bed. Powder Technol. 313, 161–168 (2017).
21. D. Spreitzer, J. Schenk, Iron ore reduction by hydrogen using a laboratory scale fluidized bed reactor: Kinetic investigation–experimental setup and method for determination. Metall. Mater. Trans. B 50, 2471–2484 (2019).
22. D. H. S. John, S. P. Matthew, P. C. Hayes, Establishment of product morphology during the initial stages of wustite reduction. Metall. Trans. B 15, 709–717 (1984).
23. X. Zhou et al., Effect of pore formation on redox-driven phase transformation. Phys. Rev. Lett. 16, 168001 (2023).
24. S. Song, P. C. Pistorius, Formation of hematite whiskers during magnetite concentrate oxidation. ISIJ Int. 59, 1765–1769 (2019).
25. S. Wu, X. Liu, J. Wu, Reduction disintegration behavior of lump ore in COREX shaft furnace. ISIJ Int. 8, 1608–1616 (2015).
26. L. Guo et al., A review on prevention of sticking during fluidized bed reduction of fine iron ore. ISIJ Int. 60, 1–17 (2020).
27. Y. Ma et al., Hierarchical nature of hydrogen-based direct reduction of iron oxides. Scripta Mater. 213, 114571 (2022).
28. D. Spreitzer, J. Schenk, Reduction of iron oxides with hydrogen–a review. Steel Res. Int. 90, 1900108 (2019).
29. J. Ilavsky et al., Development of combined microstructure and structure characterization facility for in situ and operando studies at the advanced photon source. J. Appl. Crystallogr. 51, 867–882 (2018).
30. A. Navrotsky, L. Mazeina, J. Majzlan, Size-driven structural and thermodynamic complexity in iron oxides. Science 319, 1635–1638 (2008).
31. A. Navrotsky, C. Ma, K. Lilova, N. Birkner, Nanophase transition metal oxides show large thermodynamically driven shifts in oxidation-reduction equilibria. Science 330, 199–201 (2010).
32. E. R. Jette, F. Foote, An X-ray study of the Wüstite (Fe1-xO) solid solutions. J. Chem. Phys. 1, 29–36 (1933).
33. N. Alexandra et al., Nanophase transition metal oxides show large thermodynamically driven shifts in oxidation-reduction equilibria. Science 330, 199–201 (2010).
34. G. S. Parkinson et al., Fe_3O_4(110)–(1×3) revisited: Periodic (111) nanofacets. Surface Sci. 649, L120–L123 (2016).
35. Z. Li, First-principles-based microkinetic rate equation theory for oxygen carrier reduction in chemical looping. Chem. Eng. Sci. 247, 117042 (2022).
36. D. Santos-Carballal, A. Roldan, R. Grau-Crespo, N. H. de Leeuw, A DFT study of the structures, stabilities and redox behaviour of the major surfaces of magnetite Fe(3)O(4). Phys. Chem. Chem. Phys. 16, 21082–21097 (2014).
37. F. Lu et al., Numerical simulation of iron whisker growth with changing oxygen content in iron oxide using phase-field method. Comput. Mater. Sci. 125, 263–270 (2016).
38. X. Guo, Y. Sasaki, Y. Kashiwaya, K. Ishii, Microreaction mechanism in reduction of magnetite to wustite. Metall. Mater. Trans. B 35, 517–522 (2004).
39. E. W. Thiele, Relation between catalytic activity and size of particle. Ind. Eng. Chem. 31, 916–920 (1939).
40. J. Ge et al., One-step synthesis of highly water-soluble magnetite colloidal nanocrystals. Chemistry 13, 7153–7161 (2007).
41. T. Heumann, Diffusion in Metallen: Grundlagen, Theorie, Vorgänge in Reinmetallen und Legierungen (Springer-Verlag, 1992).
42. L. E. Dresselhaus-Marais, Supplementary Raw Data for PNAS Oct 2023. OSF HOME. https://osf.io/8mbtw/?view_only=283ed02216594786af8a117b2e90e13b. Accessed 1 October 2023.